12C.5 THE MICROPHYSICAL PROCESSES OF TYPHOON NARI (2001) AT LANDFALL

Ming-Jen Yang*
National Central University, Chung-Li, Taiwan

1. INTRODUCTION

Liu et al. (1997) was the first to obtain a successful real-data explicit simulation of a tropical cyclone (TC), i.e., Hurricane Andrew (1992), using the PSU-NCAR MM5 model. The model reproduces well the hurricane track, intensity and intensity change as well as the radius of maximum winds (RMW), the hurricane eye/eyewall, and the spiral rainbands. In this study, we wish to extend the kind of TC modeling studies by conducting a cloud-resolving simulation of Typhoon Nari (2001) occurring over the northwestern Pacific Ocean, but we will focus more on its precipitation features, particularly the microphysical processes, as Nari moves across Taiwan.

Yang and Houze (1995) indicated that the simulated dynamic and kinematic features, such as rear inflow, of a squall-line type mesoscale convective system are highly sensitive to the microphysical parameterization scheme employed in the model. Wang (2002) further showed in his idealized TC simulations that the cloud structures of the simulated TC are quite sensitive to the cloud microphysics scheme; however, the intensification rate and the final intensity are not sensitive to the details of cloud microphysics parameterizations. From a series of 5-day simulation of Hurricane Bonnie (1998), Zhu and Zhang (2006) pointed out that varying cloud microphysical processes produce little sensitivity in TC's track, but different microphysics schemes generate pronounced departures in TC's intensity and inner-core structures.

Typhoon Nari struck Taiwan on September 16, 2001; it brought heavy rainfall, fresh flood, and caused severe economical and societal damage, including 92 human lives (Sui et al. 2002). Precipitation efficiency of Typhoon Nari over the ocean was discussed in Sui et al. (2005), and the flooding simulation of Nari was examined in Li et al. (2005). The first objective of this study is to investigate whether the model can reproduce the track, intensity, kinematic, and precipitation features of Typhoon Nari during its landfall on Taiwan from the given subtropical synoptic conditions, as verified against satellite, rain gauge, and radar observations (Yang et al. 2008). The second purpose is to examine the essential microphysical processes responsible of heavy rainfall associated with this landfalling storm. Through the diagnostics of simulated hydrometeor mixing ratios and latent heating/cooling fields, we wish to gain insight into the relative importance of different microphysical processes in generating Nari's heavy rainfall over Taiwan.

*Corresponding author address: Prof. Ming-Jen Yang, Department of Atmospheric Sciences, National Central University, Chung-Li, 320, Taiwan. E-mail: mingjen@cc.ncu.edu.tw

2. METHODOLOGY

The PSU-NCAR MM5 model (Grell et al. 1995) is used to simulate Typhoon Nari. The MM5 model configuration includes four nested grids with horizontal grid size of 54, 18, 6, and 2 km, respectively. The simulation is integrated for 84 h, starting from 1200 UTC 15 September and ending at 0000 UTC 19 September 2001. The initial and boundary conditions are taken from the ECMWF advanced global analysis with 1.125^{o} x 1.125^{o} horizontal resolution. The following physics options are used in the control simulation: the Grell (1993) cumulus parameterization scheme, the Reisner microphysics scheme with graupel (Reisner et al. 1998), the MRF PBL scheme (Hong and Pan 1996), and the atmospheric radiation scheme of Dudhia (1989). Note that no cumulus parameterization scheme is used on the 6 and 2-km grids.

We follow the method of Davis and Low-Nam (2001) to perform typhoon initialization. First the erroneously large vortex in the large-scale analysis is removed. Then an axis-symmetric Rankine vortex is inserted into the wind field, with the storm characteristics estimated from the best-track analysis of Central Weather Bureau (CWB) in Taiwan. When constructing the three-dimensional bogus wind, the axis-symmetric wind is vertically weighted. The vertical weighting function is specified to be unity from the surface through 900 hPa, 0.96 at 850 hPa, 0.99 at 700 hPa, 0.97 at 500 hPa, 0.85 at 300 hPa, 0.6 at 200 hPa, 0.3 at 100 hPa, and 0.1 at 50 hPa. Then the nonlinear balance equation is used to solve the corresponding geopotential height perturbation, and the hydrostatic equation is used to obtain the temperature perturbation. Moisture is assumed to be saturated within the typhoon vortex. Details in the model setup can be found in Yang et al. (2008).

The topographic effects of the Central Mountain Range of Taiwan on Nari's track, intensity, and associated rainfall amount and distributions are

examined in Yang et al. (2008) through a series of reduced-terrain sensitivity experiments. It was found that the impact of Taiwan terrain on Nari's intensity is nearly linear, with stronger storm intensity but less rainfall amounts in lower-terrain runs. On the other hand, changing the terrain heights produces nonlinear tracks, with "circled" shapes and variable movements due to different degrees of blocking effects. Parameter and diagnostic analyses reveal that the nonlinear track dependence on terrain heights results from the complex interactions between the environmental steering flow, Nari's intensity, and Taiwan's topography. The terrain-induced damping effects balance with the intensifying effects of latent heat release associated with the torrential rainfall in maintaining the near-constant storm intensity after landfall.

To further understand the terrain impact on the kinematic, thermodynamic, and microphysics features of Typhoon Nari, two 1-h periods at 0100-0200 and 1130-1230 UTC 16 September 2001 are chosen to represent the typical storm structures prior to and after Nari's landfall on Taiwan. The reason to take a one-hour time average with data intervals of 2 min is to remove the highly-transient small-scale variations and maintain the more persistent mesoscale features within the vortex circulations.

3. RESULTS

Figure 1 compares the model-simulated track of Nari from the control run to the CWB best-track estimates, using results from the 6-km, larger-area covered domain. In general, the MM5 simulates very well Nari's track, especially its landfall near Yilan at 22 h into the integration (valid at 1000 UTC 16 September 2001), albeit 3 h earlier than and 20-30 km to the north of the observed. The model also reproduces reasonably well the relatively fast and slow passage of Nari from northeast to southwest across Taiwan before and after 0000 UTC 17 September, respectively. However, the simulated track begins to deviate from the observed after 1200 UTC 18 September, leading to large displacement errors at the end of the 84-h integration.

Figure 2a shows the simulated vertical-maximum radar reflectivity field on the 2-km grid from the 1-h averaged results centered at 0130 UTC 16 September when Nari was still over the ocean, and Fig. 2b displays the 1-h averaged radar reflectivity features centered at 1200 UTC 16 September when Nari already made landfall. In particular, AB cross section in Fig. 2a is in the cross-track direction and CD cross section in Fig. 2b is in the along-track direction. It is clear that before landfall (Fig. 2a), Nari's precipitation features were very axis-symmetric, with clear eye, eyewall, and spiral rainbands. The heavy precipitation associated with a spiral rainband was further enhanced by the orographic lifting over the northern Taiwan. After landfall, Taiwan's terrain induced asymmetric pattern on the kinematic and precipitation fields, with enhanced rainfall on the windward slopes and mountain peaks over the Central Mountain Range (CMR; see Fig. 2b).

The vertical cross sections of 1-h averaged vertical velocity fields prior to and after the storm's landfall are shown in Fig. 3a and 3b, respectively. While the storm was still over ocean (Fig. 3a), strong updrafts with the intensity greater than 2.7 m s^{-1} occurred within the eyewall, narrow but intense downdrafts were located along the interface between the eye and eyewall. Wider but weaker mesoscale updrafts and downdrafts were evident in the outer spiral rainbands and trailing stratiform precipitation regions. These show the typical vertical-velocity features found in oceanic hurricanes [see Fig. 15b of Liu et al. (1997) and Fig. 3h of Liu et al. (1999)]. After Nari's landfall over northeastern Taiwan (Fig. 3b), the updrafts over the northeast branch of eyewall (x = 10~50 km in Fig. 3b) still remained vertically upright, but the updrafts over the southwestern branch of eyewall (x = -50~-10 km in Fig. 3b) "collaped" over the rugged terrain over the CMR and had a wider area coverage and stronger intensity (more than 3.3 m s^{-1}) even after the 1-h time averaging. In particular, intense downdrafts with intensity more than -1.2 m s^{-1} occurred above the sloping updrafts over land.

The vertical profiles of simulated cloud (cloud droplet and ice crystal) and precipitation (rain drop, snowflake, and graupel) mixing-ratio fields are shown in Figs 4a and 4b, respectively, for the before-landfall and after-landfall vertical cross sections. While Nari was still over the open ocean, many ice particles occurred in upper levels in association with intense updrafts in eyewalls and strong radial outflows (Fig. 4a). Abundant cloud droplets and supercooled liquid droplets were found in the intense updrafts within the eyewalls. Heavy graupel particles are mostly confined within the intense updrafts in eyewall and outer spiral rainbands (Fig. 4b). Snowflakes are maximized at the heights of 8-11 km. Raindrops are located at low levels (below the 0^{o}C isotherm), mainly produced by the melting of graupel particles and secondly generated by the melting of snowflakes.

The vertical distribution of hydrometer fields after storm's landfall on Taiwan (Figs. 5a, b) is similar to that before landfall (Figs. 4a, b), except for the fact that there were less snowflakes and graupel particles at upper level, owing to lower updraft heights and weaker convection after Nari's landfall on Taiwan. On the other hand, there is more precipitation with wider horizontal extent (in the form of rain drops) along the mountain slopes, as a result of rapid saturation as the moisture-rich airflows within Nari's vortex circulation ascending over the CMR on Taiwan.

Figure 6 illustrates the 1-h time-averaged condensational heating, evaporative cooling, depositional warming, sublimative cooling, and melting cooling along the cross-track vertical cross section before Nari's landfall. Intense condensational heating, with magnitude as strong as 56 K h^{-1}, occurs in the strong updrafts within the eyewall; one maximum of evaporative cooling is located at the 3-km level, in

association with the evaporation of rain drops, and another maximum of evaporative cooling is located at the 11-km level, owing to the evaporation of supercooled cloud droplets carried upward by the intense updrafts (Fig. 6a). Depositional warming is maximized at the 11-km height, with a gentle heating rate of 21 K h^{-1}; relatively weak sublimative cooling is widely distributed over the upper sub-saturated environment (Fig. 6b). Locally intense melting cooling (with the maximum magnitude of 3 K h^{-1}) is right beneath the 0^{o}C isotherm, with the melting-layer depth of 1-2 km.

After Nari's landfall on northeastern Taiwan, the condensational heating becomes stronger (with maximum intensity of 80 K h^{-1}) and wider in the areal extent, especially over the rugged terrain regions (Fig. 7a). With lower and weaker updrafts at upper levels, depositional warming is weaker in magnitude, compared to that before landfall (Fig. 7b). Because there is heavier rainfall over wider regions after Nari's landfall, the melting cooling is also stronger with a maximum cooling rate of 4 K h^{-1}.

The 1-h averaged total latent heating and cooling fields, the summation of all liquid-phase and ice-phased heating/cooling fields in Figs. 6 and 7, are shown in Figs. 8a and 8b, respectively, for the before-landfall and after-landfall vertical cross sections. Basically, the liquid-phase latent heating/cooling rates dominate the total latent heating/cooling rate, because there are more liquid-phase hydrometeors (cloud droplets and rain drops) compared to the ice-phase hydrometeors (ice crystals, snowflakes, and graupels) and the latent heat coefficient of evaporation is stronger than that of fusion. However, the ice-phase latent heating/cooling fields are more evident over the upper levels of eyewalls, the outer rainbands, and training stratiform precipitation regions. Condensation heating is dominant over the eyewall; evaporative cooling is evident inside the eye. Depositional warming occurs at the upper levels and evaporative cooling occurs at the lower levels in the outer stratiform rainbands (Fig. 8a). After storm's landfall, condensational heating is further enhanced within the inner core of Typhoon Nari and the terrain regions (Fig. 8b). Evaporative cooling and sublimative cooling are also enhanced over the sub-saturated environment 100-150 km away from Narti's inner core (not shown).

Reference

Davis, C. and S. Low-Nam, 2001: The NCAR-AFWA tropical cyclone bogussing scheme. *A report prepared for the Air Force Weather Agency (AFWA)*. National Center for Atmospheric Research, Boulder, Colorado.

Dudhia, J. 1989: Numerical simulation of convection observed during the Winter Monsoon Experiment using a mesoscale two-dimensional model. *J. Atmos. Sci.*, **46**, 3077-3107.

Grell, G. A., 1993: Prognostic evaluation of assumptions used by cumulus parameterizations. *Mon. Wea. Rev.*, **121**, 764-787.

Grell, G. A., J. Dudhia, and D.R.Stauffer,1995: A description of the fifth-generation Penn State/NCAR Mesoscale Model. NCAR Technical Note,122 pp.

Hong, S.-Y., and H.-L. Pan, 1996: Nocturnal boundary layer vertical diffusion in a medium-range forecast model. *Mon. Wea. Rev.*, **124**, 2322-2339.

Li, M.-H., M.-J. Yang, R. Soong, and H.-L. Huang**,** 2005: Simulating typhoon floods with gauge data and mesoscale modeled rainfall in a mountainous watershed. *J. Hydrometeor.*, **6**, 306–323.

Liu, Y., D.-L. Zhang, and M. K. Yau, 1997: A multiscale numerical study of Hurricane Andrew (1992). Part I: Explicit simulation and verification. *Mon. Wea. Rev.*, **125**, 3073–3093.

Liu, Y., D.-L. Zhang, and M. K. Yau, 1999: A multiscale numerical study of Hurricane Andrew (1992). Part II: Kinematics and inner-core structures. *Mon. Wea. Rev.*, **127**, 2597–2616.

Reisner, J., R. J. Rasmussen, and R. T. Bruitjes, 1998: Explicit forecasting of supercooled liquid water in winter storms using the MM5 mesoscaled model. *Quart. J. Roy. Meteor. Soc.*, **124**, 1071-1107.

Sui, C.-H., and Co-authors, 2002: Typhoon Nari and Taipei flood—A pilot meteorology-hydrology study. EOS, Transctions, *Amer. Geophy. Union*, **83**, 265, 268–270.

Sui, C.-H., X. Li, M.-J. Yang, and H.-L. Huang**,** 2005: Estimation of oceanic precipitation efficiency in cloud models. *J. Atmos. Sci.*, **62**, 4358–4370.

Wang, Y., 2002: An explicit simulation of tropical cyclones with a triply nested movable mesh primitive equation model: TCM3. Part II: Model refinements and sensitivity to cloud microphysics parameterization. *Mon. Wea. Rev.*, **130**, 3022–3036.

Yang, M.-J., and R. A. Houze, Jr., 1995: Sensitivity of squall-line rear inflow to ice microphysics and environmental humidity. *Mon. Wea. Rev.*, **123**, 3175-3193.

Yang, M.-J., and H.-L. Huang, 2006: A Modeling Study of Typhoon Nari (2001): Verification and topographic effects. *Preprints, The 27th Conference on Hurricanes and Tropical Meteorology*, Monterey Bay, CA, 24-28 April 2006, Amer. Meteor. Soc., 7B.2.

Yang, M.-J., D.-L. Zhang, and H.-L. Huang, 2008: A modeling study of Typhoon Nari (2001) at landfall. Part I: The topographic effects. *J. Atmos. Sci.*, in press.

Zhu, T., and D.-L. Zhang, 2006: Numerical simulation of Hurricane Bonnie (1998). Part II: Sensitivity to cloud microphysical processes. *J. Atmos. Sci*, **63**, 109-126.

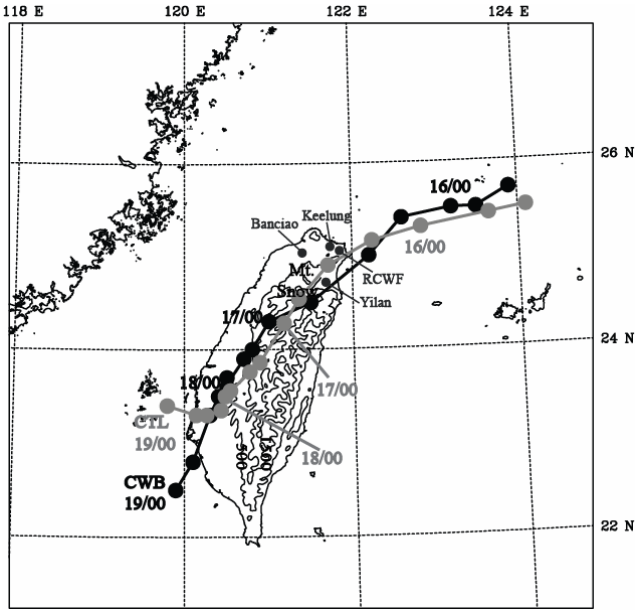

Figure 1: Comparison of the CWB best track (CWB; thick solid) and the simulated track (CTL; grey solid) of Typhoon Nari, superposed with the terrain height (thin solid) at 1000-m intervals (starting at 500-m height). Each dot denotes Nari's central position every 6 h.

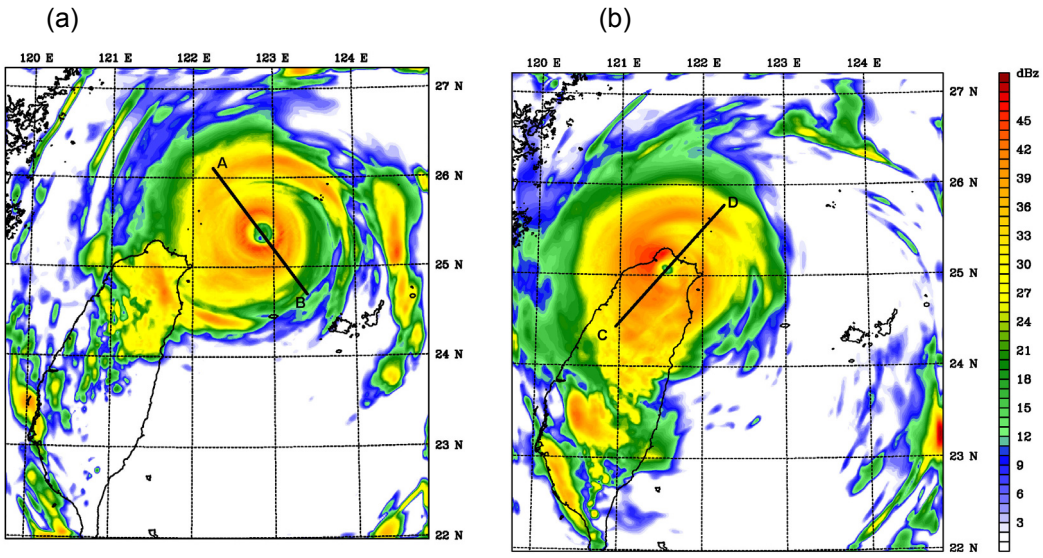

Figure 2: Vertical-maximum (CV) radar reflectivity (dBZ) from the 1-h averaged simulation results on the 2-km grid centered at (a) 0130 UTC and (b) 1200 UTC 16 September 2001. Lines AB and CD denote the locations of cross-track and along-track vertical cross sections, respectively.

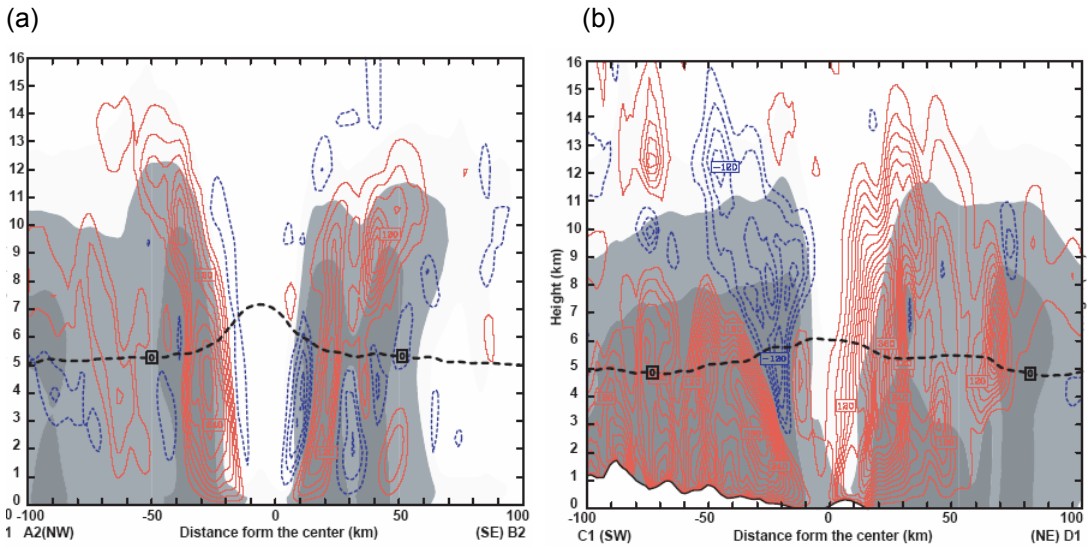

Figure 3: Vertical cross sections of vertical velocity fields from the 1-h averaged simulation results centered at (a) 0130 UTC and (b)1200 UTC 16 September 2001. Updrafts (downdrafts) are in solid blue (dashed red) contours with intervals of 0.3 m s^{-1}. Light (heavy) shading is for radar reflectivity greater than 15 (30) dBZ. Black dashed line denotes the 0°C isotherm.

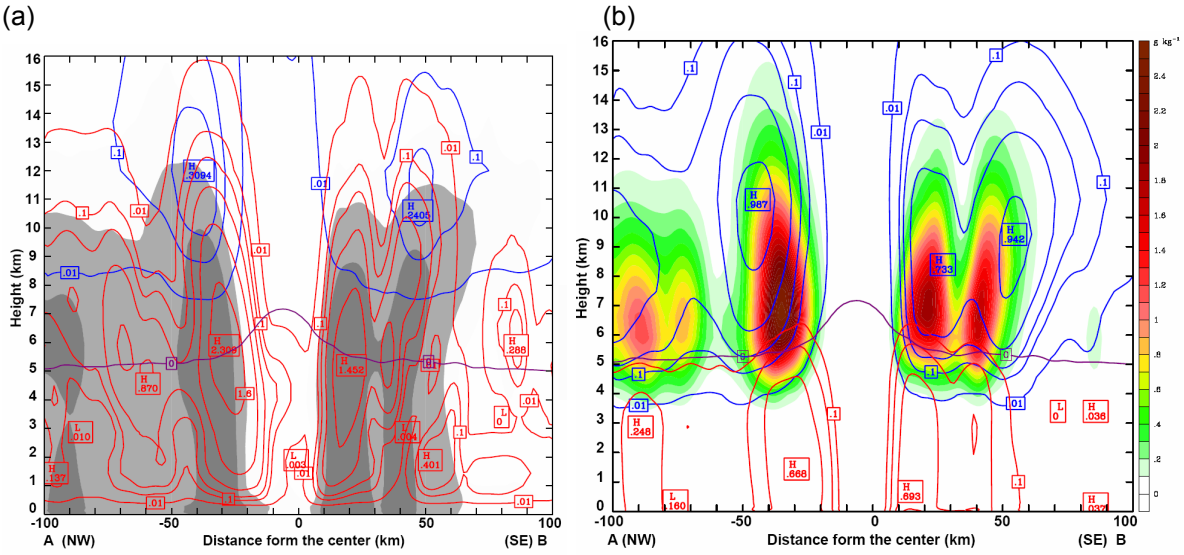

Figure 4: Before-landfall vertical cross sections of mixing-ratio fields of (a) cloud water (in red lines), cloud ice (in blue lines), and (b) rain water (in red lines), snow flakes (in blue lines), and graupel (colored) based on 1-h averaged simulation results centered at 0130 UTC 16 September 2001. Light (heavy) shading in (a) is for radar reflectivity greater than 15 (30) dBZ. Mixing-ratio fields of cloud water, cloud ice, and snowflakes are contoured at 0.01, 0.1, 0.2, 0.4, 0.8, and 1.6 g kg^{-1}. Mixing-ratio field of rain water is contoured at 0.1, 0.2, and 0.4 g kg^{-1}. Purple line denotes the 0°C isotherm.

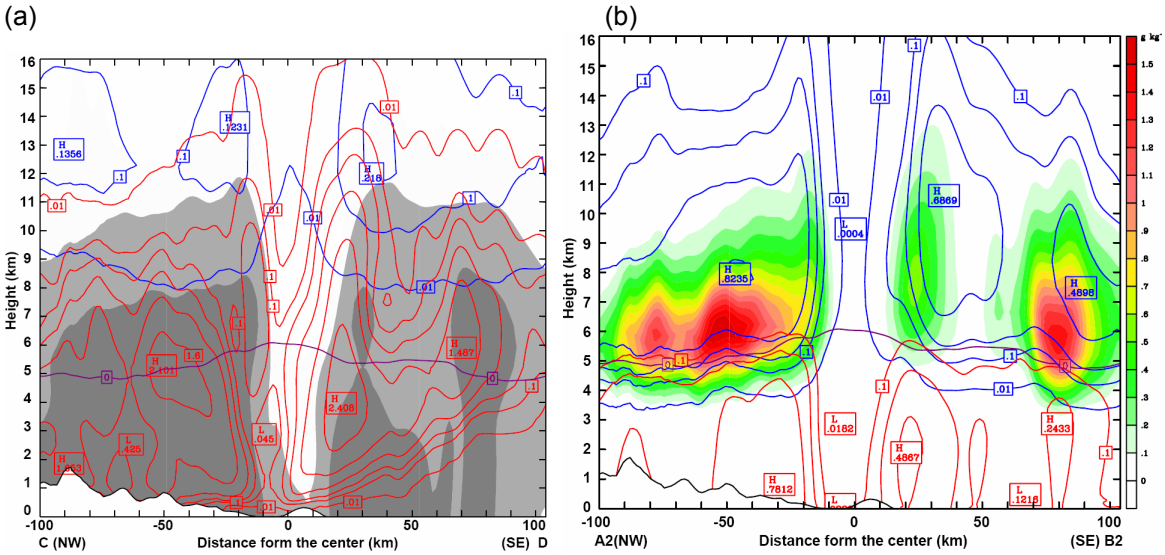

Figure 5: As in Fig. 4 except for the after-landfall vertical cross section taken from the 1-h averaged simulation results centered at 1200 UTC 16 September 2001.

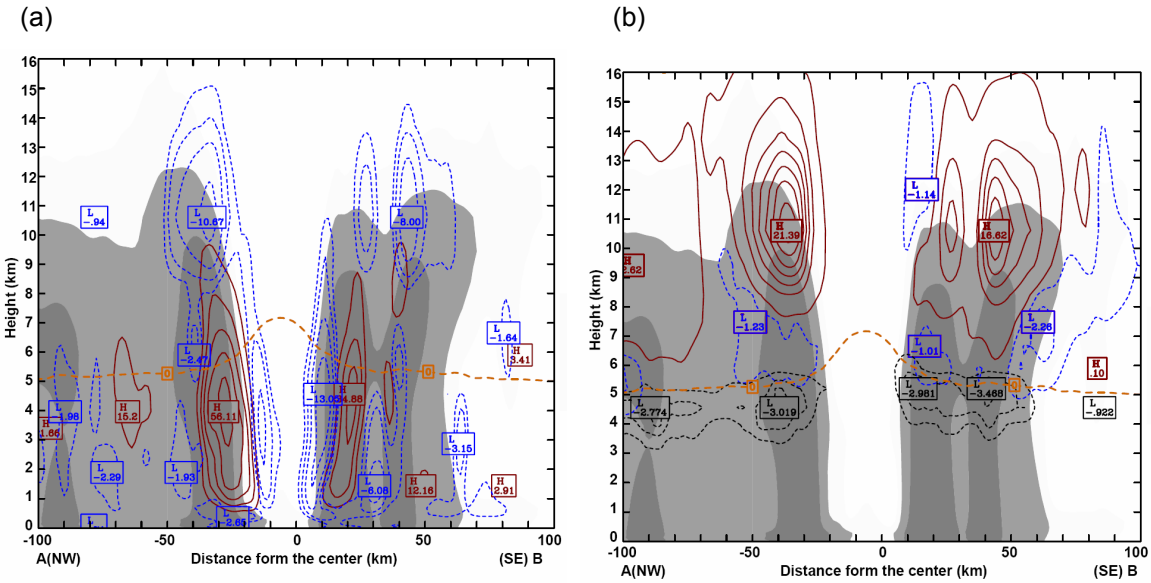

Figure 6: Before-landfall vertical cross sections of (a) condensational heating (solid black), evaporative cooling (dashed blue), and (b) depositional warming (solid black), sublimative cooling (dashed blue), and melting cooling (dotted black) based on 1-h averaged simulation results centered at 0130 UTC 16 September 2001. Condensational heating (evaporative cooling) is contoured at 10 (2) K h^{-1}; depositional warming (sublimative cooling) is contoured at 3 (1) K h^{-1}, and melting cooling is contoured at 1 K h^{-1}. Light (heavy) shading is for radar reflectivity greater than 15 (30) dBZ. Green dashed line denotes the 0^{o}C isotherm.

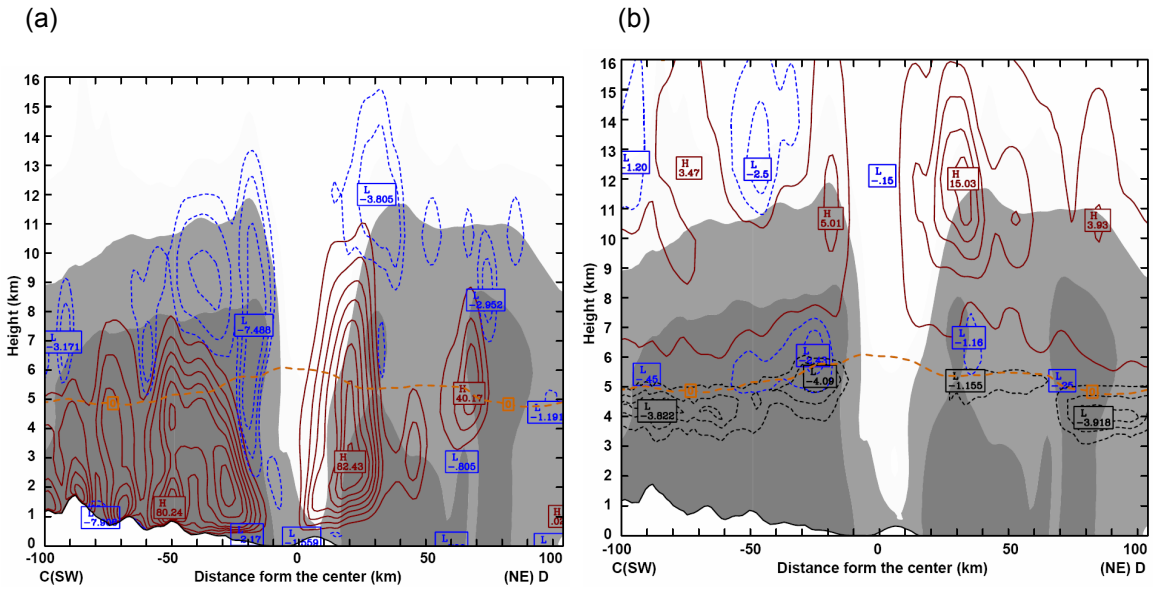

Figure 7: As in Fig. 6 except for the after-landfall vertical cross section taken from the 1-h averaged simulation results centered at 1200 UTC 16 September 2001.

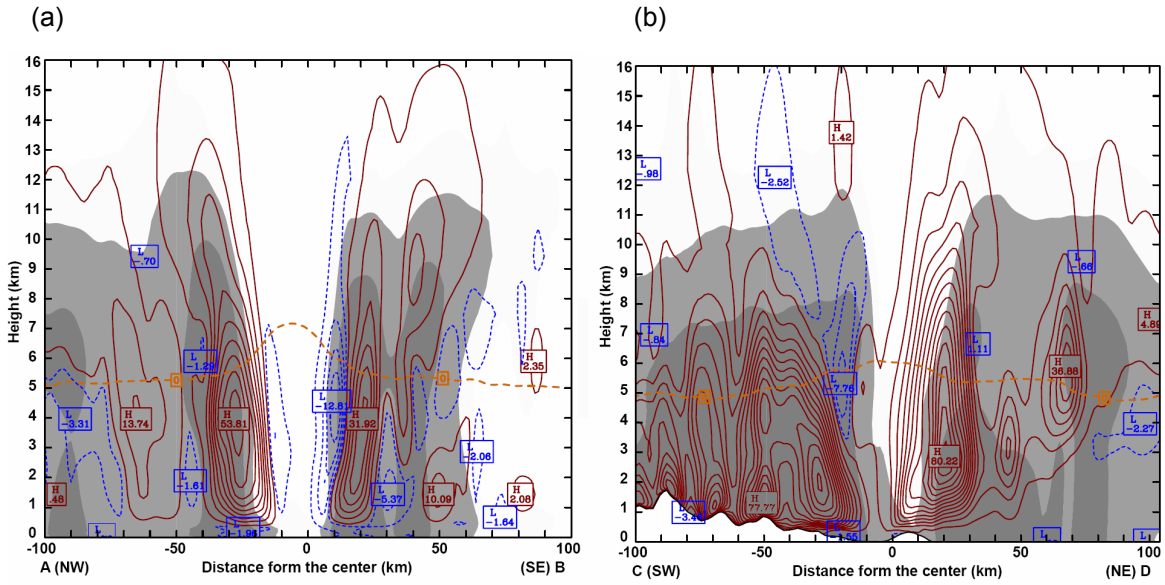

Figure 8: Vertical cross sections of total latent heating (solid black) and cooling (dashed blue) based on 1-h averaged simulation results centered at (a) 0130 UTC and (b) 1200 UTC 16 September 2001. Total latent heating (cooling) is contoured at 6 (3) K h^{-1}. Light (heavy) shading is for radar reflectivity greater than 15 (30) dBZ. Green dashed line denotes the 0^{o}C isotherm.